https://doi.org/10.5194/egusphere-2024-760
Preprint. Discussion started: 19 March 2024

A New Technique for Airborne Measurements to Quantify Methane Emissions Over a Wide Range: Implementation and Validation

Jonathan F. Dooley[a], Kenneth Minschwaner[a], Manvendra K. Dubey[b], Sahar H. El Abbadi[c], Evan D. Sherwin[c], Aaron G. Meyer[b], Emily Follansbee[b], and James E. Lee[b]

[a]Physics, New Mexico Institute of Mining and Technology, Socorro NM 87801
[b]Earth and Environmental Sciences, Los Alamos National Laboratory, Los Alamos NM 87545
[c]Lawrence Berkeley National Laboratory, Berkeley CA 94720

Correspondence: Jonathan F. Dooley (jonathan.dooley@student.nmt.edu)

Abstract. Methane (CH_4) is a powerful greenhouse gas with a global warming potential 84 times higher than carbon dioxide (CO_2) over 20 years. CH_4 is produced from many natural and anthropogenic sources which can be further classified as biogenic or thermogenic in origin. The largest biogenic sources result from anaerobic decay such as wetlands, melting permafrost, or the breakdown of organic matter in the guts of ruminant animals. Thermogenic CH_4 is generated during the breakdown of organic matter at high temperatures and pressure within the Earth's crust, a process which also produces more complex trace hydrocarbons such as ethane (C_2H_6) and propane (C_3H_8). Emissions of thermogenic CH_4 are dominated by the fossil fuel energy sector, and the presence of elevated C_2H_6 along with CH_4 can be used to distinguish oil and gas emissions from biogenic sources. This work outlines the development and deployment of an Unmanned Aerial System (UAS) outfitted with a fast (1 Hz) and sensitive ($1 - 2\,\mathrm{ppb\,s^{-1}}$) CH_4 & C_2H_6 sensor and ultrasonic anemometer. The UAV platform is a vertical-takeoff, hexarotor vehicle capable of vertical profiling to $120\,\mathrm{m}$ altitude and plume sampling across scales up to $1\,\mathrm{km}$. This system has been used for direct quantification of point sources, as well as distributed emitters such as landfills, with source rates as low as $0.04\,\mathrm{kg\,h^{-1}}$ and up to $\sim 1500\,\mathrm{kg\,h^{-1}}$. Simultaneous measurements of CH_4 and C_2H_6 mixing ratios, vector winds, and positional data allows for source classification (biogenic versus thermogenic), differentiation, and emission rates without the need for modeling or a priori assumptions about winds, vertical mixing, or other environmental conditions. The UAS has been deployed throughout the Southwest United States for system validation and targeted quantification of various sources emitting at or below the detection limits of other aircraft and satellite systems. This system offers a direct, repeatable method of horizontal and vertical profiling of emission plumes at scales that provide complementary information for regional aerial surveys as well as local ground-based monitoring.

1 Introduction

Methane (CH_4) is the second-largest contributor to anthropogenic radiative forcing and has a significantly higher Global Warming Potential (GWP) than carbon dioxide (CO_2) (Forster et al. (2007); Schneising et al. (2020); Holmes et al. (2013)). While the increased use of natural gas (primarily composed of CH_4 after processing) for energy generation has helped to reduce CO_2 emissions, supply chain leakage can reduce the environmental benefits of natural gas (Forster et al. (2007); Karion

https://doi.org/10.5194/egusphere-2024-760
Preprint. Discussion started: 19 March 2024

et al. (2013); Johnson et al. (2019)). In addition to thermogenic sources from Oil and Natural Gas (O&NG) activities, coal mining, and natural seeps, there are significant biogenic methane emissions from wetlands, biomass storage, and ruminant animals (Forster et al. (2007); Cheewaphongphan et al. (2019)). Detection of ethane—C_2H_6, the second-largest component in natural gas (Kutcherov and Krayushkin (2010); Hodnebrog et al. (2018); Forster et al. (2007); Simpson et al. (2012); Peischl et al. (2018))— is critical for source attribution, particularly when distinguishing between biogenic and thermogenic methane emissions. Kutcherov and Krayushkin (2010), Glasby (2006) and Etiope and Lollar (2013) have shown that thermogenic sources all contain some fraction ethane with methane, whereas biogenic sources contain only methane. Accurately quantifying contributions from various sources, both spatially and temporally, is an important step towards building local, regional, and global CH_4 emission estimates as well as informing policy decisions.

There are two primary methods to estimate methane emissions: statistical analysis of source activity inventories, known as 'Bottom-Up' (BU) estimations, and 'Top-Down' (TD) estimates which are based on observations constraining the atmospheric burden, often by satellites, aircraft, and/or ground-based observation networks (Heath et al. (2015); Schneising et al. (2020); Vaughn et al. (2018); Cheewaphongphan et al. (2019); Frankenberg et al. (2016)). While these methods have been used to detect methane leaks(Frankenberg et al. (2016)) and have played an important role in environmental regulation and policy (Heath et al. (2015)), the two methods show persistent discrepancies (Vaughn et al. (2018); Peischl et al. (2018); Cheewaphongphan et al. (2019)). Many BU/TD estimation methods typically represent only a snapshot in time and do not effectively account for temporal variations such as diurnal and seasonal variability. Multiple studies have shown that O&NG methane emissions vary significantly in time (Lavoie et al. (2017); Johnson et al. (2019); Vaughn et al. (2018)) indicating that frequent and repeated measurements may help to reduce and constrain uncertainties in emissions monitoring (Schneising et al. (2020); NAS2018).

A common method for estimating GHG emissions using aircraft is a mass balance approach (Hiller et al. (2014); Karion et al. (2013, 2015); Lavoie et al. (2015)), which uses GHG concentration measurements upwind and downwind of target sources to isolate source methane enhancements from background concentrations (Chen et al. (2016); Frankenberg et al. (2016); Schwietzke et al. (2017); Johnson et al. (2019)). These measurements can be collected from aircraft transecting the source plume (Frankenberg et al. (2016); Schwietzke et al. (2017)) or by simultaneous measurements using similar instruments installed upwind & downwind of the sources (Chen et al. (2016); Gisi et al. (2012)). The accuracy of the latter method depends on a relatively constant wind speed and direction during data collection. Therefore, it is imperative to have accurate knowledge of the target area's principal wind conditions to properly install the instrument, and only those data obtained under favorable meteorological conditions can be used to accurately estimate the flux (Chen et al. (2016)). Detailed modeling of meteorology over large domains (e.g., WRF) of data from multiple solar spectrometers has also been used to infer emissions but is uncertain when flows are complex (Viatte et al. (2017); Heerah et al. (2021)). Ground-based differential measurements can be useful for characterizing sources with higher spatial resolution than typical space-based instruments such as TROPOMI's $10 \times 10\,\mathrm{km}^2$ horizontal resolution (Schneising et al. (2020)). However, the required site analysis and the cost to deploy and maintain multiple ground-based sensors limit the number of surveys that can be conducted, especially in secluded, rural areas.

While satellites can monitor CH_4 at a global scale, most remote sensing instruments must estimate wind speed and direction as well as the Boundary Layer (BL) height in order to calculate the source emission rate (Alexe et al. (2015); Frankenberg

https://doi.org/10.5194/egusphere-2024-760
Preprint. Discussion started: 19 March 2024

et al. (2005); Parker et al. (2011); Kort et al. (2014); Schneising et al. (2020)). The estimated detection thresholds for satellite instruments is in the range of 100-10,000 $\mathrm{kg\,h^{-1}}$(Jacob et al. (2022)), and recent work by Sherwin et al. (2023) indicates a lower detection limit of between 500 and 1000 $\mathrm{kg\,h^{-1}}$ for most satellite systems. Similar to satellites, aircraft CH_4 detection systems require a priori wind information around the source location. However, some aircraft systems are able to infer the BL height and have a minimum detection thresholds of 2-10 $\mathrm{kg\,h^{-1}}$ due to proximity and higher spatial resolution (Duren et al. (2019)). Combined measurements using both aircraft and complementary satellite data result in more robust TD emission estimates, but scheduling and implementing contemporaneous measurement from both air and space can be prohibitively difficult and time-consuming. Ground-based detection systems are the most straightforward and accessible methods, but effective site monitoring is highly dependent on wind directions. Column-averaged measurement techniques using Fourier Transform Spectrometers (FTS) also require BL height estimations and are unable to provide vertical profiles of source plumes. There is a need for direct, repeatable, and cost-effective methods for detecting and quantifying CH_4 emissions from relatively small sources ($< 1\,\mathrm{kg\,h^{-1}}$), which do not require a priori assumptions.

This paper details the integration, testing, and initial results of a new methane flux measurement system. It utilizes a compact mid-IR spectrum analyzer and lightweight anemometer onto a commercially available Unmanned Aerial Vehicle (UAV) for efficient, repeatable flux measurement and characterization of anthropogenic sources. This novel design combines rapid sampling of chemical and meteorological data with a mobile platform capable of vertical and horizontal profiling relative to target sources, for high resolution spatial sampling of emission plumes.

2 System Design

The full Unmanned Aerial System (UAS) is depicted in figure 1. It includes four main components: (*1*) mobile Mid-IR methane and ethane sensor (Aeris MIRA Pico) (*2*) lightweight 3D vector wind and environmental sensor (Anemoment Trisonica Mini) (*3*) Unmanned Aerial Vehicle (*UAV*, DJI Matrice 600 Pro) (*4*) onboard computer for system monitoring and data collection.

2.1 Onboard Sensors

2.1.1 Methane and Ethane Sensor

The MIRA (Mid-InfraRed Analyzer) Pico Leak Detection System (LDS) developed by Aeris Technologies employs a solid state laser and multi-pass absorption cell with a spectral band pass between 2.5 and 4.7 µm. The wide spectral range allows for simultaneous mixing ratio measurements of both CH_4 and C_2H_6 with a precision of $1\,\mathrm{ppb\,s^{-1}}$ and $0.5\,\mathrm{ppb\,s^{-1}}$, respectively (MIRAManual2019; Scherer (2017)). The response time is a function of the gas flow rate through the cell, which can be adjusted via the speed of a small gas pump; flow rates for our system correspond to a response time of ~1.5 s based on laboratory tests of the decay in pulsed gas releases. The MIRA has been used extensively on the ground including controlled release tests at Colorado State University's (CSU) METEC facility to find and quantify leaks (Travis et al. (2020)).

https://doi.org/10.5194/egusphere-2024-760
Preprint. Discussion started: 19 March 2024

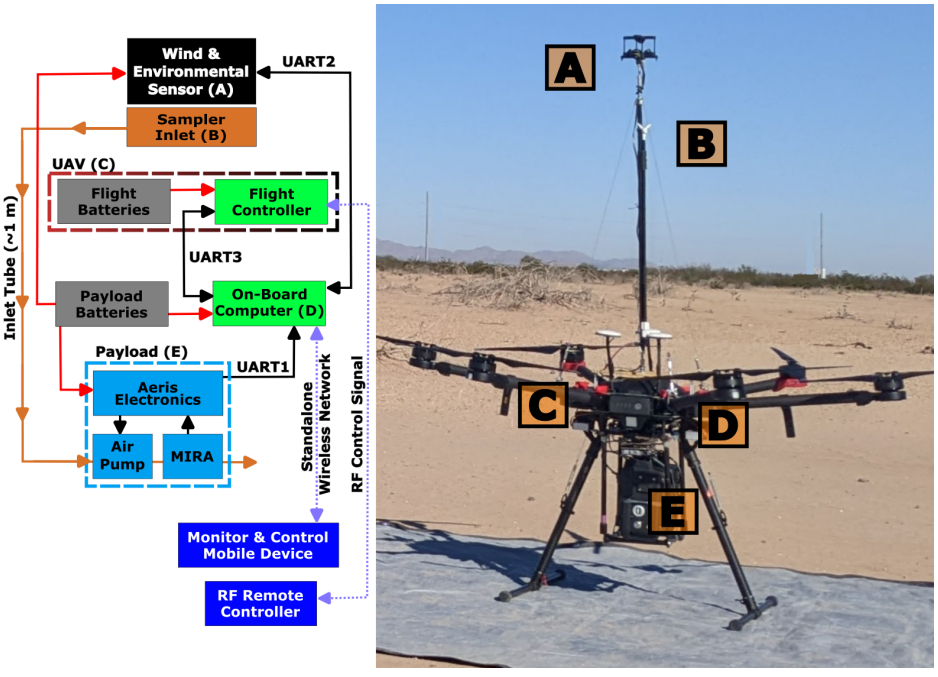

Figure 1. Unmanned Aerial System (UAS) design overview. (*Left*) System block diagram: (*A*) Trisonica Mini Weather Sensor (TWS), (*B*) dual-opening sampler inlet, (*C*) Matrice 600 Pro Unmanned Aerial Vehicle (M600P UAV), (*D*) Raspberry Pi 4 on-board computer, and (*E*) Aeris MIRA Pico methane and ethane sensor. (*Right*) Flight-Ready UAS collecting ground data prior to takeoff. TWS and sampler inlet (*A* and *B*) mounted on a carbon fiber tube mast above the M600P's rotor wash.

2.1.2 Onboard Anemometer and Weather Sensor

In addition to gas mixing ratios, direct flux quantification requires measurements of vector winds, temperature, and pressure. The system includes an ultra-light, 3D sonic anemometer: the Trisonica Mini Weather Sensor (TWS) by Anemoment has a mass of 50 g with a volume of less than 450 cm^3 (TWSDatasheet2022; TWSManual2018). Direct, in situ measurements of vector winds during flight removes the need to assume consistency in speed & direction as the UAS rapidly changes location and altitude throughout each flight. Additionally, environmental measurements can also be used as a way to detect and adapt to unsafe conditions during flights (Hollenbeck et al. (2018)). The TWS senses vector winds ($|\boldsymbol{u}|$), temperature (T), and pressure (P) at 5 Hz with an accuracy of $\delta|\boldsymbol{u}| = 0.35\,\mathrm{m\,s^{-1}}$, $\delta T = 2\,\mathrm{C}$, and $\delta P = 10\,\mathrm{hPa}$, respectively (see table 1).

2.1.3 Unmanned Aerial Vehicle (UAV)

The UAV (DJI Matrice 600 Pro, M600P) is a hexarotor vertical takeoff and landing aircraft that is capable of flying with relatively large payload masses of up to 5.5 kg. This powerful and mobile platform became commercially available in 2014 and has been used in a variety of scientific and commercial applications (McKinney et al. (2019); Villa et al. (2016); Hollenbeck et al. (2018)). The M600P can be remotely piloted up to a distance of up to 5 km at a maximum altitude of 125 m above ground

https://doi.org/10.5194/egusphere-2024-760
Preprint. Discussion started: 19 March 2024

level. Flight times depend on factors such as payload mass, winds, and flight pattern. Under typical winds of 2–4 $\mathrm{m\,s^{-1}}$ and the standard total payload mass of ~3 kg, total flight times range between 18 and 25 min. We employ dual battery packs that are cycled between flying and charging in the field, allowing for about one flight per hour.

The M600P is controlled via proprietary software & firmware with an expansive API for telemetry logging and flight control (MIRAManual2019). However, the reliance on proprietary software limits system customizability and sensor integration (see section 2.2). While it is possible to automate flight plans for the M600P, it is more important for the operator to maintain control of the UAS throughout the entire flight to account for changing or unexpected flight conditions.

2.2 Sensor Integration

Each of the three main devices (MIRA Pico, TWS, and M600P) has its own output data stream that must be separately parsed and then temporally synchronized with the other streams. The M600P does not support the use of DJI's proprietary 'Payload SDK' — firmware enabling sensor data to be transmitted along with the RF control signal. Therefore, remote monitor and control of the fully-integrated UAS is handled independently of the M600P via an onboard device for both acquisition and transmission. A 4$^{\mathrm{th}}$ generation Raspberry Pi (RPi) single board computer is the ideal choice due to its size, weight, and programmability via the Linux Kernel. The RPi is powered independently via a 10 Ah payload battery (see figure 1) allowing for ground-based data collection between flights, typically while the UAV batteries are charging.

2.2.1 Payload Sensor Mounting

The both the RPi onboard computer and MIRA Pico mount to the M600P underside as shown in figure 1. The UAV achieves flight by funneling air downwards to create thrust, constantly displacing air around the vehicle's body in the process (DJIM600P2018). Computational fluid dynamics simulations carried out by McKinney et al. (2019) determined that the Matrice 600 Pro causes disturbances up to 5 m below the UAV's center of mass; however, the magnitude of the disturbances drops off quickly at a height of 60 cm above the UAV body.

The TWS mounts to a mast made of lightweight, carbon fiber tubing (0.5 in diameter) anchored near the UAV's center of mass. This places the TWS ~85 cm above the UAV and above the shallow inflow layer generated by propellers during normal flight. At this height above the propellers, air disturbances are below the noise floor of the TWS (~0.1 $\mathrm{m\,s^{-1}}$) or easily calibrated out during data processing. A ~1 m section of flexible tubing connects the payload's gas cell to a dual-opening sampling port approximately 80 cm above the body of the M600P. This tubing introduces a phase lag of ~2 s between the measured CH_4 concentration time series and the TWS data, which is accounted for in the calculation of instantaneous fluxes.

While the TWS has an integrated magnetometer to measure heading, this device is intended for stationary deployment in an open location where averaging of compass readings can result in a relatively accurate direction. However, any magnetic disturbance created from adjacent devices or operating motors perturb the heading measurements. In contrast, the M600P has a triple redundant positioning system with an accuracy of $< 3°$ at 200 Hz. The TWS must be physically aligned with the more accurate heading data from the M600P's Inertial Measurement Unit (IMU) to accurately calculate static-frame vector winds (more in Section 2.3).

https://doi.org/10.5194/egusphere-2024-760
Preprint. Discussion started: 19 March 2024

In order to ensure proper alignment, the M600P is set up facing North with the TWS mounting point tightened so that the anemometer's North arm is facing the same direction. The MIRA Pico and Onboard Computer are both mounted under the body of the UAV as shown in figure 1. Initial UAV test flights revealed that payload mounting at this location improves flight performance, especially during takeoff and landing, due to the lower center of mass.

2.3 Relative Wind Adjustments

The Trisonica Mini Weather Station (TWS) is designed for static installation with one arm facing north (TWSDatasheet2022) and will therefore produce incorrect results when the device's heading ('yaw', ψ) is not a multiple of 2π (TWSDatasheet2022; TWSManual2018; Hollenbeck et al. (2018)). In addition, the motion of the UAV during data collection induces an apparent wind that is folded into the TWS wind measurement. Transforming the raw TWS vector wind measurements ($\boldsymbol{u_m} = [u_m, v_m, w_m]$) to Earth-fixed coordinates therefore requires accurate, real-time measurements of ψ and UAV velocity ($\boldsymbol{V_s}$).

In order to transform raw TWS wind data to static-frame vector winds, we apply a standard Galilean transformation $\boldsymbol{u} = \boldsymbol{R}(\phi)\boldsymbol{u_m} + \boldsymbol{V_s}$ or

$$\begin{bmatrix} u \\ v \\ w \end{bmatrix} = \begin{bmatrix} \cos(\phi) & \sin(\phi) & 0 \\ -\sin(\phi) & \cos(\phi) & 0 \\ 0 & 0 & 1 \end{bmatrix} \begin{bmatrix} u_m \\ v_m \\ w_m \end{bmatrix} + \begin{bmatrix} V_x \\ V_y \\ V_z \end{bmatrix} \tag{1}$$

Here, $\boldsymbol{u_m} = [u_m, v_m, w_m]$ are the TWS-measured vector winds, $\boldsymbol{u} = [u, v, w]$ is the corrected wind speed in Earth-fixed coordinates, and $\boldsymbol{V_s} = [V_x, V_y, V_z]$ is the instantaneous UAS velocity. $\boldsymbol{R}(\phi)$ is the counter-clockwise (CCW) Euler rotation matrix about the vertical axis ($\hat{z}$) where ϕ is the heading (yaw) of the M600P. Rotations around the $\hat{y}$ and $\hat{x}$ axis — caused by variations in UAV pitch (θ) and roll (φ), respectively — are neglected since changes in θ and φ are negligible during steady, level flights. A time series of the TWS-measured raw winds during a typical flight is shown in figure 2, along with the derived static-frame vector winds based on the M600P headings and velocities throughout the flight.

2.4 Background Mixing Ratio Estimation

While the MIRA Pico is highly sensitive with a large dynamic range ($\sim 20\,\mathrm{ppb} < \chi_{\mathrm{CH_4}} < 4000\,\mathrm{ppm}$) (MIRAManual2019; Meyer et al. (2022); Follansbee et al. (2024)), there are observable levels of semi-periodic drift in the measured mixing ratios for both hydrocarbons at the ppb level. This effect is especially noticeable for $\chi_{\mathrm{C_2H_6}}$, partly because ambient mixing ratios for C_2H_6 are generally $\sim 100\times$ smaller than CH_4. In addition to these instrumental drifts, the raw concentration measurements (χ) may reflect actual changes in background mixing ratios. Nearby point sources to do not directly influence these background variations; instead they may be related to regional-scale emissions and meteorological influences such as winds and stability at the mesoscale level. Both of these effects contribute to structure in the measured background (χ_0), which must be accurately quantified in order to isolate enhancements from the target source. This background variability generally occurs over periods

https://doi.org/10.5194/egusphere-2024-760
Preprint. Discussion started: 19 March 2024

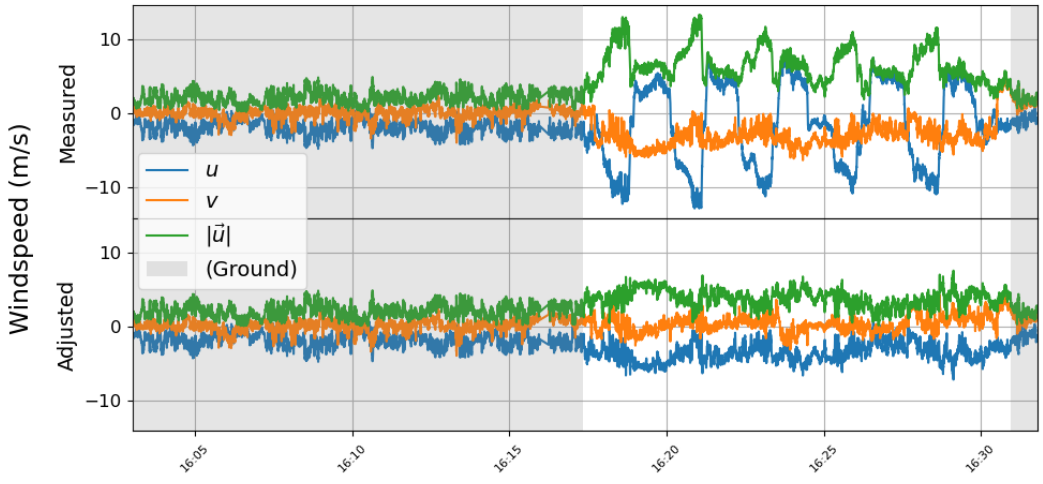

Figure 2. Raw measured vector winds: (top) and heading/velocity corrected vector winds (bottom) before, during, and after flight. Pre- and post-flight ground wind speeds at the takeoff location highlighted in gray.

of minutes and is independent between χ_{CH_4} and $\chi_{C_2H_6}$, so that direct comparison prior to baseline removal can be misleading, especially over longer period datasets.

The UAS measurement strategy involves repeated cross-wind sampling of the plume downwind of a target source (as discussed in more detail in section 3.1). The resulting time series of mixing ratio data contains a number of finite-width enhancements superimposed on a slowly varying background, as shown in figure 3. χ_0 is estimated by fitting a polynomial to the measurements outside the plume. After extensive testing, the procedure outlined in figure 3 proved to be the most effective method of filtering inter-plume samples.

The raw χ timeseries is initially 3-point-smoothed ($\widetilde{\chi}$) to decrease the effect of noise in the identification of the plume edges. The gradient of $\widetilde{\chi}$ is then used to detect abrupt changes to $\widetilde{\chi}$ which are indicative of the UAS entering or exiting the higher-concentration plume, as shown in 3. Samples where $\nabla\widetilde{\chi}$ is greater than a specified threshold (γ) are determined to be 'in-plume'. For this analysis, we determined a threshold of $0.2 * \sigma$ reliably distinguished between in-plume and 'background' periods. $\pm 0.2\sigma$ in figure 3 and in the subsequent analysis of measurements presented here). This filter removes the majority of the inter-plume samples, leaving behind the 'background' samples which vary at a much lower frequency. The gradient filter output is then thresholded to remove any remaining inter-plume measurements; the final output samples are from outside the target plume (background measurements, $\widetilde{\chi}_{bg}$) and a variable order polynomial ($\deg(3)$ in figure 3) is fit to these samples. The regression coefficients that best fit $\widetilde{\chi}_{bg}$ are then applied to the original χ timestamps to estimate χ_0 for each independent hydrocarbon and dataset.

https://doi.org/10.5194/egusphere-2024-760
Preprint. Discussion started: 19 March 2024

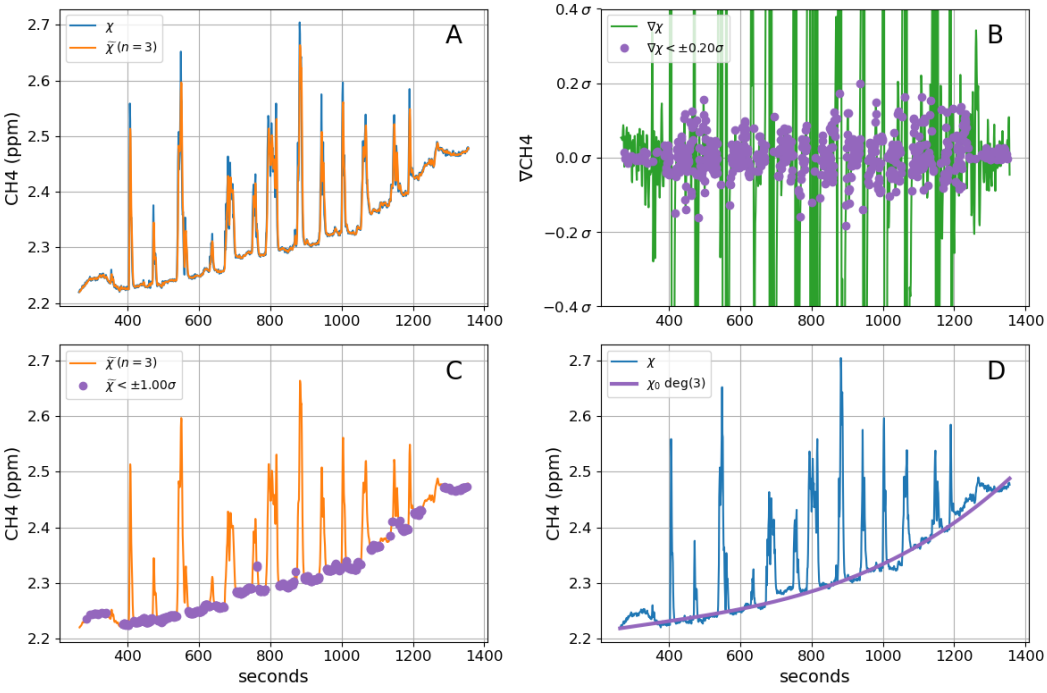

Figure 3. Time series of methane measurements during a typical flight, illustrating the procedure for baseline estimation and removal. The flight involved multiple cross-sections through the downwind plume of a known point emitter, and the plume enhancements in methane are visible as large spikes in the methane time series. (*A*) 3-point smooth raw data. (*B*) gradient filter to detect the majority of in-plume samples. (*C*) split remaining samples into segments and remove statistical outliers from each segment. (*D*) 3rd order polynomial fit using remaining samples; resultant regression coefficients used with initial (non-smoothed) raw data samples used to estimate baseline.

2.5 Plume Simulations

Idealized Gaussian plume models are a reasonable first approximation for an emission plume inverse modelling (e.g., Jacob et al. (2022); Shah et al. (2019); Stockie (2011); Meyer et al. (2022); Follansbee et al. (2024)).

$$C(x,y,z) = \frac{Q}{|\boldsymbol{u}|} \cdot \frac{1}{2\pi\,\sigma_y(x)\,\sigma_z(x)} \cdot \exp\left[-y^2/\left(2\sigma_y(x)^2\right)\right] \cdot \exp\left[-(z-H)^2/\left(2\sigma_z(x)^2\right)\right] \tag{2}$$

The Gaussian plume equation for the mass density of a gas (C, units of $\mathrm{kg\,m^{-3}}$) downwind of a point source emitter is Q is emission rate ($\mathrm{kg\,s^{-1}}$), $\boldsymbol{u}$ is the constant horizontal wind speed ($\mathrm{m\,s^{-1}}$), σ_z & σ_y are standard deviations for Gaussian distributions, in units of meters, which are generally derived using stability classes (Seinfeld and Pandis (2006)). H is the height of the source (m). C is the estimated increase in gas density at position x (directly downwind, centerline), y (horizontal from centerline), and z (vertical from centerline) given in meters. It is important to make the distinction between the mass density, C ($\mathrm{kg\,m^{-3}}$), and the volume mixing ratio χ ($\mathrm{mol\,mol^{-1}}$) measured by the MIRA Pico. The conversion between the

https://doi.org/10.5194/egusphere-2024-760
Preprint. Discussion started: 19 March 2024

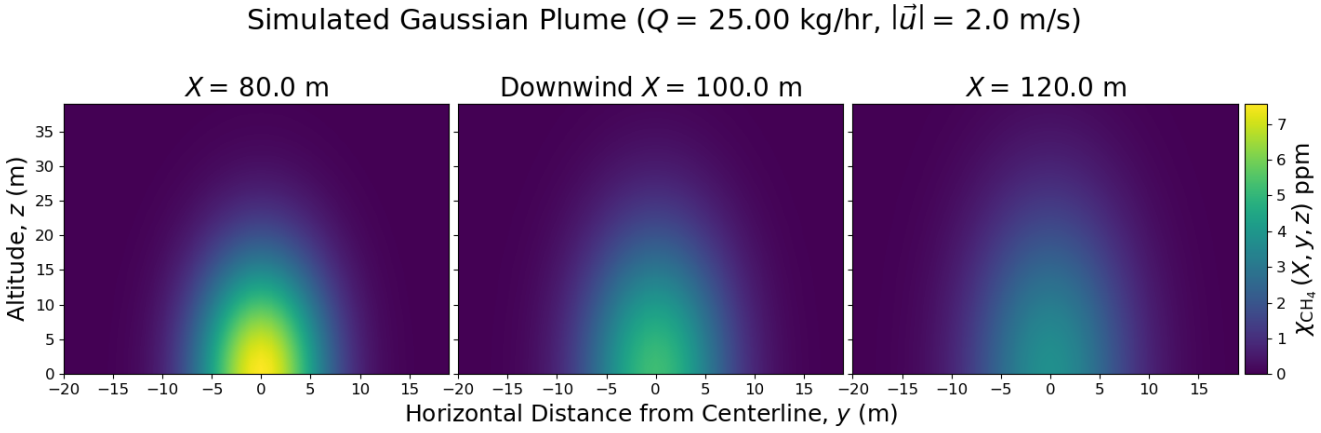

Figure 4. Cross-sections of modelled Gaussian plume under conditions of low wind (2 m s) and high solar insulation (stability class "A" from Woodward (2010)). Each panel depicts the Gaussian plume cross-section at distance X downwind of the source. The horizontal distance, y, is with respect to plume centerline and the vertical distance z is above ground level. The plume model assumes a steady wind field and constant emission rate from the source.

two is $C = \eta\rho\chi$ where η is the ratio of molar masses of the gas to that of air, and ρ is the air density ($\mathrm{kg\,m^{-3}}$). Figure 4 shows cross-sections of a Gaussian plume simulated at three downwind distances from a $25\,\mathrm{kg\,h^{-1}}$ point source. Mean winds in this case are ~$2\,\mathrm{m\,s^{-1}}$ and the stability class corresponds to high solar insolation. As expected, the simulated plume becomes more dispersed, and broadens both horizontally and vertically with increasing distance from the source. Plume enhancements in methane range between 1 and 5 ppmv, which are easily detectable with this system, and the horizontal and vertical scales (~50 m, ~30 m) are readily accessible to the UAS.

3 Deployment

This section describes the preliminary flight preparation for the UAS based on the modelling and UAV flight time. If both emissions from the target source and surrounding environmental winds are relatively steady during the M600P's 15 to 25 min flight time, then Gaussian models offer a reasonable approximation the expected structure that could be observed in methane enhancements downwind of the source (Seinfeld and Pandis (2006); Shah et al. (2019); Stockie (2011)). The Gaussian modeling discussed in the previous section helps to guide and describe the sampling strategy for target sources, but it should be emphasized that source fluxes reported in this work do not involve Gaussian inverse modelling from direct measurements (see section 3.2).

https://doi.org/10.5194/egusphere-2024-760
Preprint. Discussion started: 19 March 2024

3.1 Flight Pattern

The full UAS setup and pre-flight checks can be completed in under $15\,\mathrm{min}$ and any certified remote pilot, or person under the supervision of a certified pilot (ACS2021), can maneuver the UAS around target sources for direct plume sampling. The flight time of ~$20\,\mathrm{min}$ constrains the types of flight patterns that can be used to quantify source emission rates.

In order to maximize the number of in-plume samples within a relatively short flight period, our strategy is to remain downwind of the source and fly horizontal 'transects' perpendicular to the mean wind direction. This curtain or boustrophedonic flight is perpendicular to the average wind direction, and involves multiple cuts through the plume in order to measure both the in-plume concentrations, χ, and the ambient or background concentrations used to determine χ_0. Each individual transect through the downwind plume is at a relatively constant altitude and horizontal velocity between 2 and $5\,\mathrm{m\,s^{-1}}$, depending on the wind conditions and proximity to the source. Transects are typically $50\,\mathrm{m}$ to $1\,\mathrm{km}$ in length, depending on terrain, wind variability, and source distribution and downwind distance. Extended sources and measurements collected at larger downwind distances from the source require longer transects to ensure that the dispersing plume gets fully traversed during each transect. The ability to quickly adjust altitude between each of the individual transects allows for direct measurements of the plume's vertical structure in addition to the horizontal dispersion.

Direct measurements of a source plume with the MIRA Pico sensor requires the UAS to be physically maneuvered downwind of the source. While a steady-state Gaussian plume model can be used for flux inversions (e.g., Jacob et al. (2022); Shah et al. (2019); Stockie (2011); Seinfeld and Pandis (2006); Woodward (2010); Bhattacharya (2013)), these models represent plume dispersion probabilities which are not generally observed in the superposition of horizontal transects through the plume. During direct measurements, large-scale turbulence in the wind flow results in changes to the plume's size and relative location throughout the measurement period. Based on simple scaling arguments, we expect that plume variability is largest in the horizontal plane due primarily to wind directional variability. Figure 5 shows multiple simulated transects through a Gaussian plume's downwind cross-section in the case of a steady-state flow. We simulate the stochastic variability in the plume by introducing random shifts in centerline between each of the temporally separated transects, which can be seen at the bottom of Figure 5. This pattern is generally more consistent with our observations in comparison to the steady state model. However, the stochastic model shows that total plume flux is unaffected by horizontal plume displacements, provided that the integral is taken along horizontal transects.

3.2 Direct Flux Quantification

The data collected from a single flight is broken into K individual transects through the source's downwind plume, each transect representing data collected at a nearly-constant altitude, z, and non-zero horizontal velocity, $\boldsymbol{V_s}$, while intersecting the plume. The altitude, z, is only adjusted between transects with the UAS outside the plume (measuring ambient or background concentrations).

Mass balance estimation techniques such require knowledge of the wind speed perpendicular to the direction of travel (transect crosswind). Optimally, each transect would therefore be perpendicular to the mean horizontal wind direction ($\overline{\boldsymbol{u}}$), but

https://doi.org/10.5194/egusphere-2024-760
Preprint. Discussion started: 19 March 2024

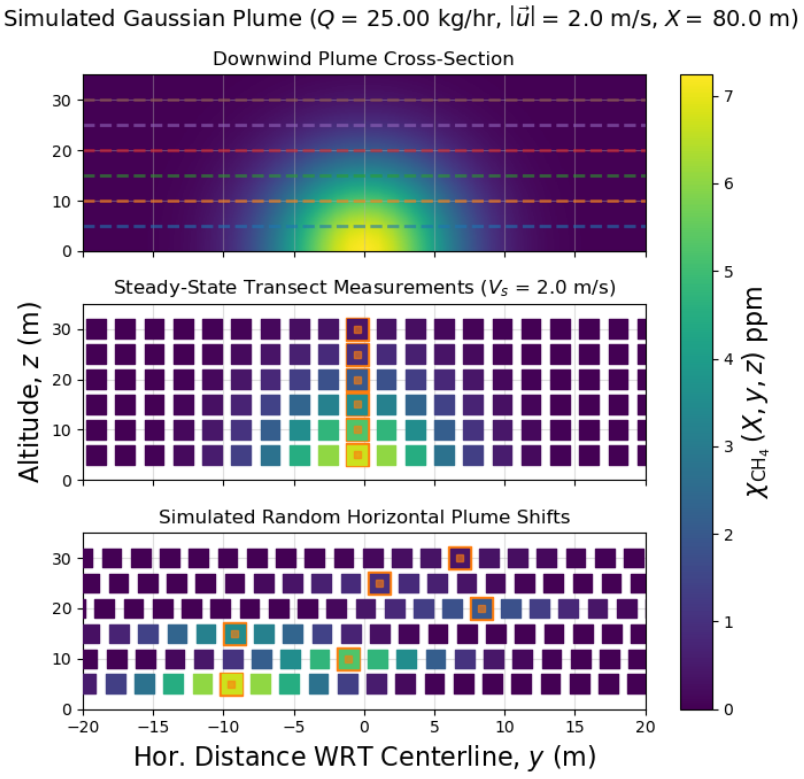

Figure 5. Simulated flight through Gaussian plume: (*top*) cross-section of plume X meters directly downwind of source, simulated transects shown as dotted lines. (*middle*) Resample of modelled cross-section at constant horizontal transect velocity V_s. (*bottom*) Random shifts in centerline horizontal position, simulating variable wind conditions and temporally separated plume transects.

local topography, changing wind fields, and flight safety considerations often result in an angle other than 90° between $\boldsymbol{V_s}$ and $\boldsymbol{u}$. Therefore, it is important to first define a unit vector, $\hat{n}$, perpendicular to the direction of travel. Equation 3 shows the system of equations used to calculate this unit vector.

$$\begin{cases} \|\hat{n}\| = n_x^2 + n_y^2 = 1 \\ \boldsymbol{V_s} \cdot \hat{n} = V_x\, n_x + V_y\, n_y = 0 \end{cases} \tag{3}$$

V_x and V_y are the instantaneous UAS velocities defined previously. The transect crosswind, a measure of windspeed perpendicular to the UAS transect, is $(\boldsymbol{u} \cdot \hat{n})$. Maintaining a constant heading and horizontal velocity during flights proved difficult during periods of irregular and shifting winds. Direct measurements of $\boldsymbol{u}$ and $\boldsymbol{V_s}$ are variable between samples so that $\hat{n}$ is required to constrain the flux calculation with respect to each transect.

https://doi.org/10.5194/egusphere-2024-760
Preprint. Discussion started: 19 March 2024

Each of the K horizontal transects gets processed individually to calculate the intermediate transect-integrated flux f_k (equation 4). This is the horizontal integral of the measurements along each transect with units of mass flux rate per unit vertical distance ($\mathrm{kg\,s^{-1}\,m^{-1}}$).

$$f_k = \eta \sum_{i=0}^{n-1} \rho_i (\chi - \chi_0)_i (\boldsymbol{u} \cdot \hat{n})_i \Delta s_i = \sum_{i=0}^{n-1} (C - C_0)_i (\boldsymbol{u} \cdot \hat{n})_i \Delta s_i \tag{4}$$

$\eta\rho(\chi - \chi_0) = (C - C_0)$ is the background-adjusted mixing ratio, $\Delta s = |\boldsymbol{V_s}|\Delta t = \sqrt{V_x^2 + V_y^2}$ is the distance between samples ($\Delta t \approx 1\,\mathrm{s}$), and ρ and η are defined previously.

The total flux, F_{tot}, is then calculated through integrating the sum of f_k and the vertical distance between physically adjacent transects, Δz_k (equations 5 and 6).

$$\Delta z_k = \begin{cases} |\overline{z}_{k+1} - \overline{z}_k|/2 + 3\,|\overline{z}_k|/4 & \overline{z}_k = \min(\overline{z}_0, \ldots, \overline{z}_{K-1}) \\ |\overline{z}_{k-1} - \overline{z}_k| & \overline{z}_k = \max(\overline{z}_0, \ldots, \overline{z}_{K-1}) \\ (|\overline{z}_{k-1} - \overline{z}_k| + |\overline{z}_{k+1} - \overline{z}_k|)/2 & \text{otherwise} \end{cases} \tag{5}$$

$$F_{tot} = \sum_{k=0}^{K-1} (f_k\, \Delta z_k) \tag{6}$$

Adjustments to the vertical integral step Δz_k are taken at the bottom and top transects to account for extrapolation to the ground and above the flight pattern. A typical flight downwind of a natural gas point source is shown in figure 6. This flight is composed of eleven horizontal transects over a period of approximately $11\,\mathrm{min}$. The transects were flown approximately $130\,\mathrm{m}$ downwind (roughly south-southeast) of the methane point source with a known emission rate of $3.42 \pm 0.01\,\mathrm{kg\,h^{-1}}$.

3.3 Precision and Uncertainties

Figure 7 presents the distribution of CH_4 and C_2H_6 baseline estimate residuals ($\varepsilon_0 = \chi_0 - \widetilde{\chi}_{bg}$) taken from two test flights downwind of known natural gas point sources. The 3σ confidence interval (99.7%) is approximately $20\,\mathrm{ppb}$ for CH_4 and $2\,\mathrm{ppb}$ for C_2H_6 enhancement detection.

Table 1 gives the measurement uncertainties for the major components of the UAS. The precision on the baseline estimate and associated uncertainties for each sensor lead to an estimated lower quantification threshold of $\sim 7\,\mathrm{g\,h^{-1}}$ during standard flight conditions.

https://doi.org/10.5194/egusphere-2024-760
Preprint. Discussion started: 19 March 2024

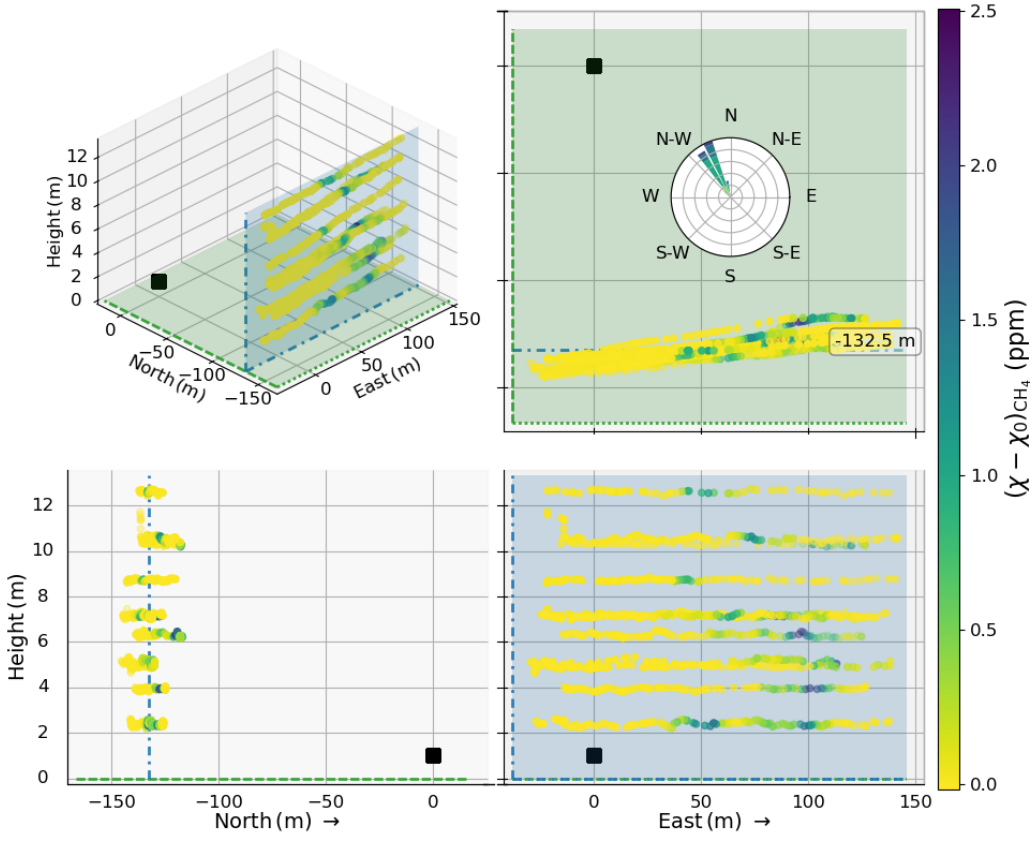

Figure 6. Plume transect flight pattern viewed from east (bottom left), south (bottom right), and from above (top right). Approximate source location marked with black square. The windrose plot (top left) shows the Earth-fixed wind in the horizontal direction.

https://doi.org/10.5194/egusphere-2024-760
Preprint. Discussion started: 19 March 2024

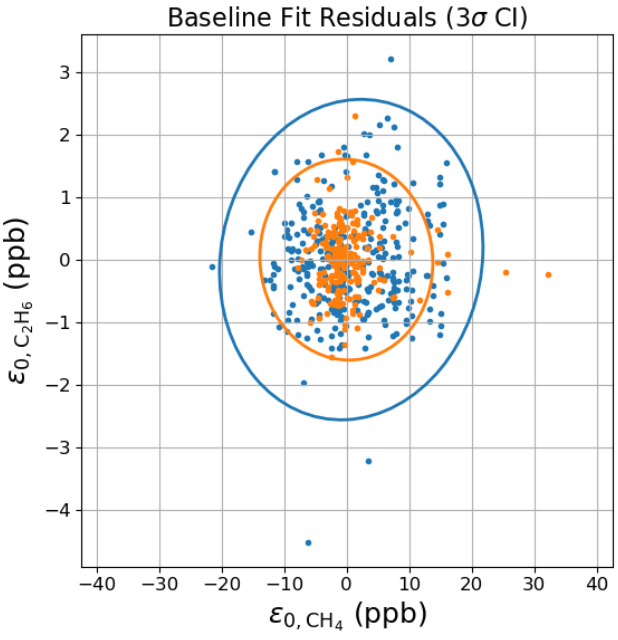

Figure 7. Residuals CH_4 and C_2H_6 baseline polynomial fit (outlined in figure 3) for two independent datasets, overlaid with 3σ confidence ellipse.

Sensor	Measurement	Uncertainty	Units
TWS	Pressure	1000	Pa
TWS	Temperature	2	C
TWS	Wind Speed	0.2	m/s
M600P GNSS	Horizontal Velocity	0.05	m/s
M600P IMU	Heading (Yaw)	0.05	rad
M600P IMU	Pitch, Roll	0.017	rad
MIRA Pico	Methane	10	ppb
MIRA Pico	Ethane	1	ppb
RPi RTC	Timestamp	100	ms
Pipeline	Methane	20	ppb
Pipeline	Ethane	10	ppb

Table 1. Sensor uncertainties TWSDatasheet2022; DJIM600P2018; MIRAManual2019

https://doi.org/10.5194/egusphere-2024-760
Preprint. Discussion started: 19 March 2024

4 Analysis

In Fall of 2022, the NMT team participated in a single-blind controlled release validation campaign in Casa Grande, Arizona, USA (Sherwin et al. (2023); El Abbadi et al. (2023)). While this validation campaign focused on larger-scale aircraft and satellite system validation, it was a unique opportunity to quantify the accuracy for this method of direct methane flux quantification. The UAS was deployed multiple times around the controlled release location during two separate, three-day validation trips: October 10–12 and November 14–16, 2022. Multiple flights at various times throughout the daily testing window (between 10:00 and 14:00 MST most days) measured concentrations downwind of the release stack.

Due to battery life and charging limitations, the UAS typically can accommodate about one flight per hour. Additionally, the flux quantification method described in section 3.2 relies on relatively stable wind fields around the source, optimally between 2 and $6\,\mathrm{m\,s^{-1}}$. Suboptimal environmental conditions and unforeseen instrumentation issues resulted in the rejection of the majority October 2022 flights from the analysis process. The November 2022, 3-day campaign produced a total of 12 flights, 8 of which were during times of low-variability windfields and good flight conditions to allow for reliable flux quantification.

It is important to note that, at the time of this campaign, the UAS flight pattern and quantification method was still in active development. While the NMT team quantified and submitted flux estimates during the single-blind and partially-blinded phases of the unblinding process (described in El Abbadi et al. (2023)), the final unblinded metered emissions were invaluable to debug and update the initial quantification process, ultimately leading to the numerical integration outlined in section 3.2. Here, we present the analysis of the quantification results informed by the unblinded, ground truth-methane flow rates.

Figure 8 shows the comparison between UAS-calculated flux and the corresponding unblinded metered emissions from 8 independent November 2022 flights. The metered rates, taken to be the ground truth emission rates, range from 1.7 to $1500\,\mathrm{kg\,h^{-1}}$. This broad range of emission rates highlights the system's dynamic range and the fitted linear regression shows the quality of emission estimates compared to the one-to-one agreement with metered rates (dotted line). Our method of flux quantification shows reasonable agreement with the expected emission rates above $1\,\mathrm{kg\,h^{-1}}$. However, the results suggest a systematic underestimation of the emissions which is not correlated to number of transects or windspeeds during flights. One interpretation of these results is that our field measurements could represent a reasonable lower bound to the true emission rate of the source.

4.1 Other Sources

The deployment strategy for this UAS is designed to quantify emissions from targeted local sources such as O&NG wells and manure storage/biogenic lagoons. With a limited operational distance and flight time, larger distributed sources (such as large-scale dairies and agricultural centers) are difficult to properly quantify using the numerical integration technique described in section 3.2. However, smaller-scale municipal waste facilities with heterogeneous emission profiles can be quantified as long as the UAS is able to fully, and repeatedly, transect the complex and irregular plumes downwind of the facility.

https://doi.org/10.5194/egusphere-2024-760
Preprint. Discussion started: 19 March 2024

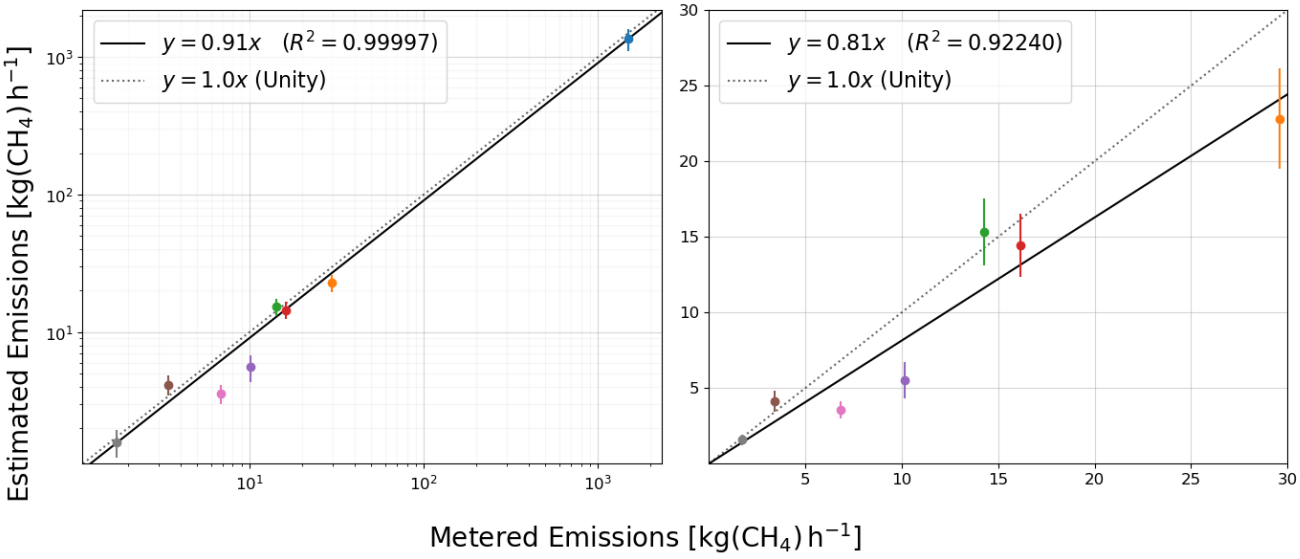

Figure 8. Comparison of UAS CH_4 flux calculation verses Metered Emissions reported by El Abbadi et al. (2023) and Sherwin et al. (2023). Both plots show 8 individual flights during the November 2022 field campaign with 1σ error bars. Linear regression fit shown as solid line for comparison with the idealized one-to-one fit corresponding to perfect agreement between UAS and Metered data (dotted line). *Left* Logarithmic plot highlighting UAS's large dynamic range. *Right* Linear plot focused on emission rates below detection limits of most aircraft quantification methods; linear regression fit does not include emission rates above $100\,\mathrm{kg\,h^{-1}}$.

4.1.1 Municipal Waste Facility

During the course of system development and testing, the UAS was deployed around a local Municipal Waste Facility (MWF) in Socorro, NM. This location serves a county population of approximately 16,300 with multiple cells over an area of 45 hectares. Larger facilities studied by Olaguer et al. (2022) and Lan et al. (2015) reported emission rates between 85 and $> 2000\,\mathrm{kg\,h^{-1}}$; this much smaller local facility, however, was expected emit at rates less than $10\,\mathrm{kg\,h^{-1}}$ (Olaguer et al. (2022); Bogner and Matthews (2003)). The low emission rate and temporal heterogeneity, likely due to changes in cell activity, is evident across the multiple visits between Spring 2022 and Summer 2023. The flight path from one such flight can be seen in figure 9.

In comparison to flights downwind of point sources such as O&NG wells or controlled NG releases (figure 6), the flight pattern and in figure 9 was positioned about $0.5\,\mathrm{km}$ downwind of the source and involved plume transects up to ~$500\,\mathrm{m}$ long, and over an altitude range of up to $50\,\mathrm{m}$. In addition, the methane enhancements are about a factor of 10 lower than in figure 6, and the plume is distributed over a larger area and centered at a higher altitude. Nevertheless, the overall plume structure allows for the same flux analysis as discussed for the localized NG point sources above. The measured methane emission rate for this flight was $1.12 \pm 0.67\,\mathrm{kg\,h^{-1}}$.

https://doi.org/10.5194/egusphere-2024-760
Preprint. Discussion started: 19 March 2024

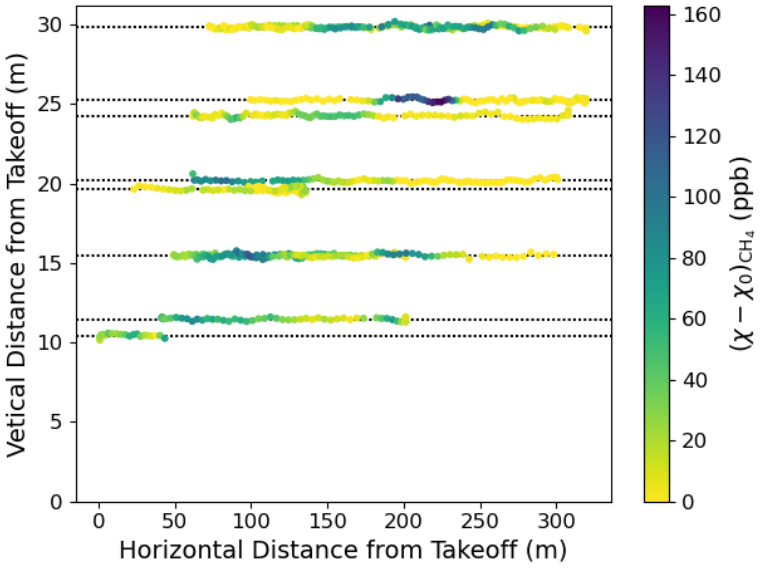

Figure 9. Example flight, split into individual transects, from landfill in New Mexico. The landfill itself is composed of activate and inactive cells distributed over and area of approximately $45\,\mathrm{ha}$, resulting in a non-uniform downwind plume profile. Comparison with localized 'point source' presented in figure 6, longer horizontal transects across a wider vertical range are required to measure the multiple distributed and highly variable emitters.

4.1.2 Orphan Well

During April 2023, the UAS was also deployed around an 'orphaned well' located in Hobbs, New Mexico, USA. This site has been out-of-use for more than two decades and was in the initial phase of being plugged when visited in April 2023. A detailed analysis of data from this field campaign is presented in Follansbee et al. (2024). The observed plume structure was similar to that shown in figure 6, but mean wind speeds were much larger and methane plume enhancements were $\sim 400\,\mathrm{ppb}$, roughly between the range of plume enhancements shown in figures 6 and 9. Three downwind flights yielded consistent fluxes in the range of 0.3 to $0.5\,\mathrm{kg\,h^{-1}}$ (Follansbee et al. (2024)).

4.1.3 Wastewater Treatment Plant

Wastewater Treatment Plants (WWTPs) are a known source of biogenic methane emissions via biodegradation of pollutants by anaerobic bacteria (Song et al. (2023)). The small town of Socorro, NM has a local Wastewater Treatment plant that processes less than one million gallons per day (MGD) so that its contribution to anthropogenic methane is relatively quite low (when compared to O&NG and agricultural operations). However, the low emission rate of this location was useful for testing of the UAS's lower detection and quantification limits.

https://doi.org/10.5194/egusphere-2024-760
Preprint. Discussion started: 19 March 2024

A timeseries of measured CH_4 and C_2H_6 concentrations from a short flight in August 2023 is shown in figure 10. While the in-plume CH_4 concentration levels peak at around $40\,\mathrm{ppb}$, the measured C_2H_6 levels do not exceed the sensor's noise floor of $< 1\,\mathrm{ppb}$ while passing through the plume. The lack of any correlation between C_2H_6 & CH_4 is strong evidence that the measured plume is from anaerobic digestion at the WWTP and is not contaminated by another source. The emission rate for the flight shown in figure 10 is estimated to be $68.7\,(+171.5, -61.7)\,\mathrm{g\,h^{-1}}$.

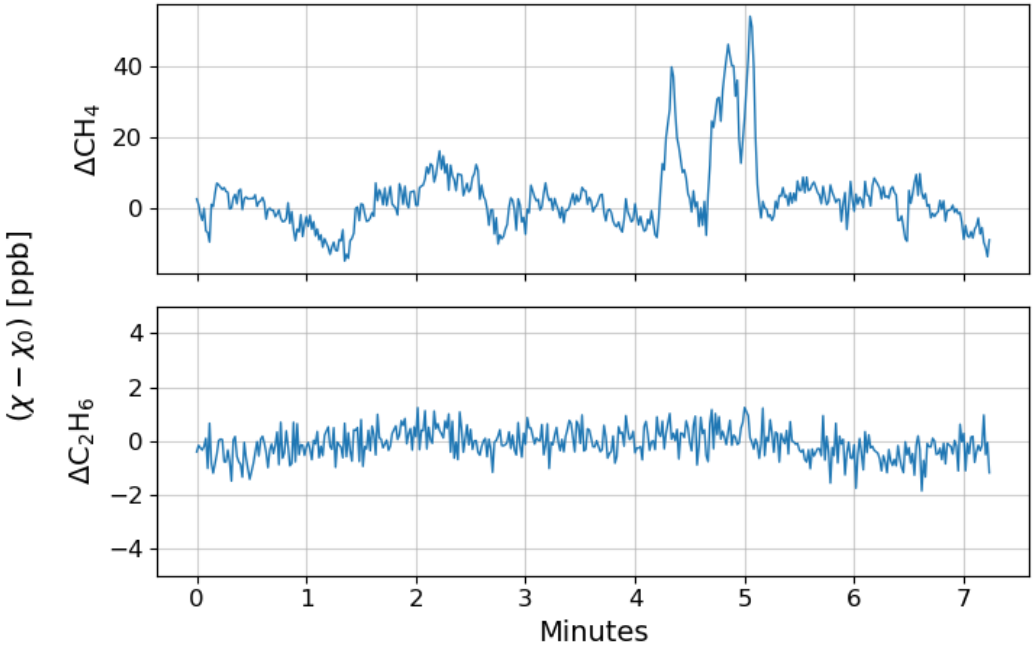

Figure 10. Timeseries of methane and ethane mixing ratios, with background subtracted as described in section 2.4, from a flight downwind of the City of Socorro wastewater treatment plant in August, 2023. The mean winds were $\sim 5\,\mathrm{m\,s^{-1}}$ and the solar insolation corresponded to stability class "B" due to partial cloud coverage (Woodward (2010)). The biogenic plume was intercepted on two transects separated by about $40\,\mathrm{s}$, as seen in the methane timeseries about 4-5 $\mathrm{minutes}$ into the flight.

4.2 Source Attribution

As discussed in Section 1, simultaneous measurements of both CH_4 and C_2H_6 is useful for source classification as either biogenic or thermogenic. In addition, there are varying ratios of trace hydrocarbons found in thermogenic natural gas sources, and C_2H_6 is the second-most dominate compound in refined natural gas (Peischl et al. (2018); Hodnebrog et al. (2018); Kutcherov and Krayushkin (2010); Glasby (2006); NAS2018; Forster et al. (2007); Hansen et al. (2000); Meyer et al. (2022)). Therefore, the ratio of C_2H_6 to CH_4 can be used to estimate the percentage of non-methane compounds in an O&NG plume and distinguish between sources.

https://doi.org/10.5194/egusphere-2024-760
Preprint. Discussion started: 19 March 2024

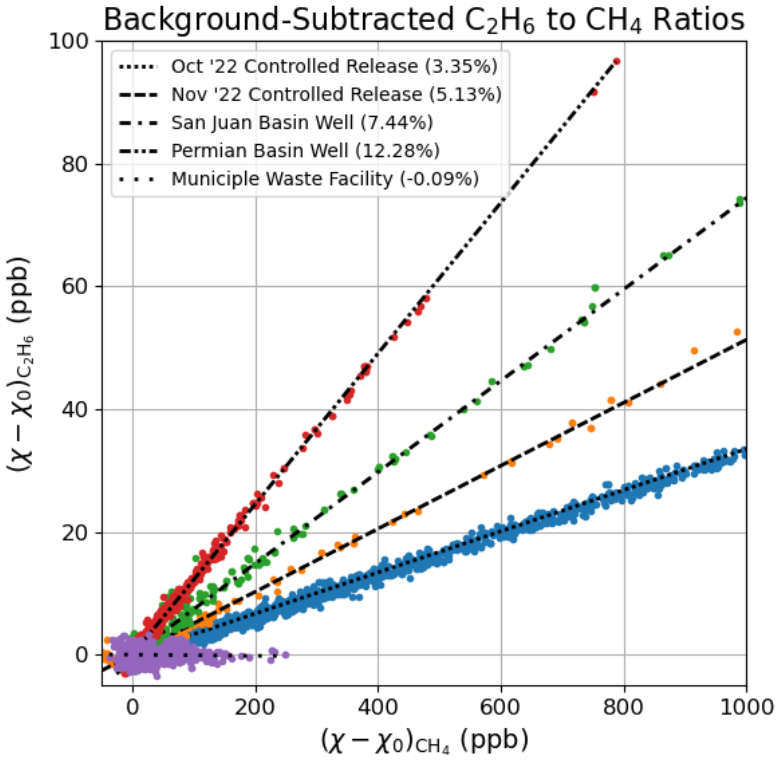

Figure 11. Ethane & Methane enhancement ratios from multiple independent field tests at different sites. *October and November 2022 Controlled Releases*: are two independent multi-day field campaigns in Casa Grande, AZ during a controlled NG release. *San Juan Basin Well*: Multiple flights near an active well-head in Cuba, NM. *Permian Basin Well*: three independent flights downwind of a an orphan well in Hobbs, NM, *Municipal Waste Facility* is a relatively small waste disposal location near Socorro, NM.

Figure 11 shows the ratio of measured C_2H_6 and CH_4 mixing ratios from five different field measurements around various sources, including the municipal waste facility discussed in section 4.1.1. Multiple downwind plume measurements showed a negligible C_2H_6 content ($< |0.2\%| \Delta C_2H_6/\Delta CH_4$) from this biogenic source. Consistent with figure 9, the magnitude of plume CH_4 from the MWF is much lower in comparison to the thermogenic methane sources we have sampled. Figure 12 highlights the dynamic range of the UAS, which is able to detect CH_4 enhancements of as little at $20\,\mathrm{ppb\,s^{-1}}$ (after baseline removal, Section 2.4). Additionally, the UAS has demonstrated the ability to measure much larger concentrations of more than $40,000\,\mathrm{ppm}$ (empirically determined based on MIRA Pico saturation levels during AZ validation flights).

The two different controlled release campaigns in Fall 2022 were about one month apart, and these data are segregated in figure 12. The measured percentages are in agreement with the contemporaneous CH_4 concentration measurements reported by the controlled release team (El Abbadi et al. (2023)). The same ratio of C_2H_6 to CH_4 was measured across all flights during

https://doi.org/10.5194/egusphere-2024-760
Preprint. Discussion started: 19 March 2024

the first release and similarly during the second campaign, though the ethane content was noticeably different during the second campaign.

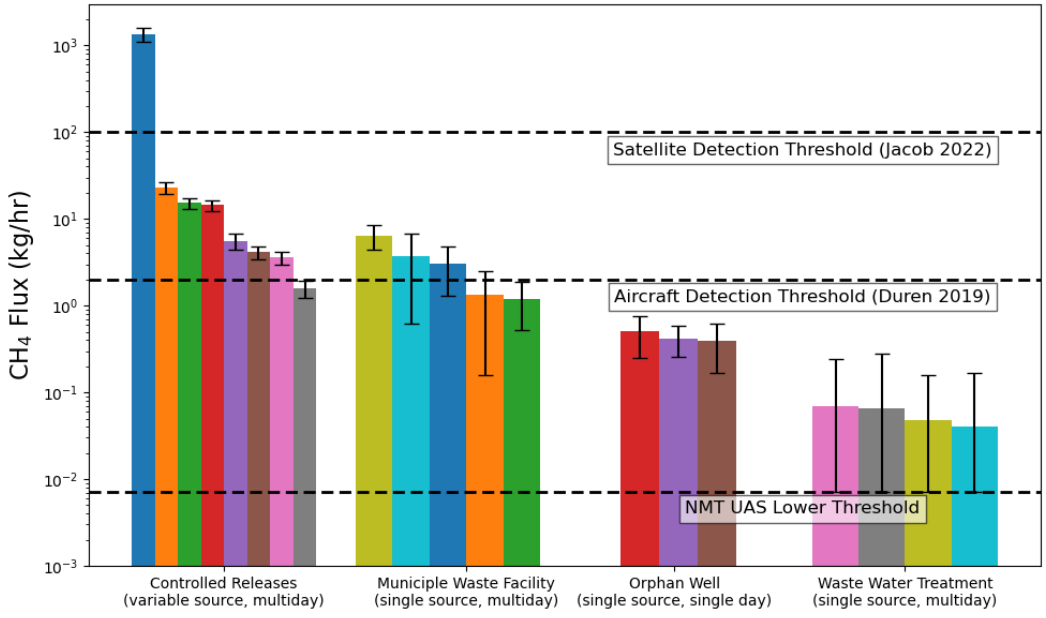

Figure 12. Comparison of estimated Methane flux from various anthropogenic sources. The UAS has a large dynamic range capable of quantifying emission rates from smaller sources (less than $1\,\mathrm{kg\,h^{-1}}$). Horizontal dashed lines show the absolute lowest detection limits for satellite and aircraft quantification methods (Jacob et al. (2022); Duren et al. (2019)) with respect to the estimated lower limit of this system ($\sim 0.007\,\mathrm{kg\,h^{-1}}$, see section 3.3)

Emissions of unrefined NG from the orphan well discussed in section 4.1.2 contained a smaller fraction of CH_4 due to the presence of other compounds such as H_2S, so that it is incorrect to approximate the C_2H_6 ratio in figure 11 as the non-CH_4 percentage. However, this unique C_2H_6/CH_4 ratio was consistent across all orphan well flights, and in good agreement with ground-based systems deployed at the same site (Follansbee et al. (2024)); larger ethane content is due to the unrefined natural gas seeping from the unused well. (Stolper et al. (2018)). Furthermore, measurements of unrefined NG from a leaking O&NG well in the San Juan Basin, obtained in October 2023, showed a distinct ratio from that of the orphan well from the Permian Basin. The San Juan Basin is primarily a coal producing region and therefore has a noticeably lower C_2H_6 content compared to the Permian Basin, the latter region being primarily composed of oil. Thus, each of the sources shown in Figure 12 had a unique and consistent C_2H_6 ratio which can be used to characterize and differentiate multiple sources based on this percentage. This is in agreement with the findings of Meyer et al. (2022).

https://doi.org/10.5194/egusphere-2024-760
Preprint. Discussion started: 19 March 2024

5 Conclusions

Our results demonstrate the capabilities of this integrated UAS package, along with associated flight strategies and data analysis methodologies, to quantify and characterize methane emitters across a range of spatial scales (point to ~1 km). Through direct, in situ measurements of CH_4 mixing ratios and vector winds within the downwind plumes of target sources, this system can be used to robustly quantify emission source strengths spanning more than three orders of magnitude. Figure 12 presents a summary of flux measurements from different sources, ranging from large (~1500 kg h^{-1}) emissions in controlled release experiments, to the very low emissions (0.040 kg h^{-1}) observed from a local WWTP. Large error bars on the four independent WWTP flights are consistent with the error associated for other low-emission. As noted in the figure, our UAS has the capability to quantify emission rates up to and above the lower limits of satellite and aircraft CH_4 monitoring systems; thus it is useful for contemporaneous source quantification to help constrain and bridge the gap between ground-based and top-down measurement systems. The lower measurement bound for methane fluxes is estimated to be ~0.007 kg h^{-1}, and it is determined primarily by the precision of the methane measurement and uncertainties associated with the background determination and plume enhancement.

The primary limitations of our UAS measurement approach are related to meteorological conditions. Optimum mean wind speeds are in the range 2-6 m s^{-1}. Wind speeds below 2 m s^{-1} have been shown to produce less reliable fluxes due to higher variability in the plume position and shape, while winds above 6 m s^{-1} are too strong for safe flights with this UAS. The steadiness of wind directionality can also be a factor, although it is a much less severe constraint than speed provided that the flight pattern is sufficiently wide to intersect the plume on every transect. Proper deployment also requires access for takeoff and landing within 1 km of the source, and the target source's location must also be known to within a few kilometers. Thus, although this system is not optimized for wide-area surveys, it is well suited for site quantification of known sources such as O&NG wells or processing facilities, small dairies and municipal waste facilities, and wastewater treatment plants.

Competing interests. The contact author has declared that none of the authors has any competing interests.

Acknowledgements. Support for instrumentation and UAV equipment provided in part by the New Mexico Tech Office of Research. This project has benefited from collaborations with the New Mexico Bureau of Mines, the New Mexico Petroleum Recovery Research Center, and Los Alamos National Laboratory. We thank the NMT Facilities Management Office for their support of field measurements during the course of this project.

Special thanks to operators of the controlled release in Casa Grande, AZ; recognizing the team members who contributed to field operations during the October and November 2022 testing periods and to processing the ground-truth data that was provided (in alphabetical order by last name): Adam R. Brandt, Philippine M. Burdeau, Yuanlei Chen, Zhenlin Chen, Sahar H. El Abbadi, Jeffrey S. Rutherford, Evan D. Sherwin. From Rawhide Leasing (operating the gas equipment): Mike Brandon, S.M.

https://doi.org/10.5194/egusphere-2024-760
Preprint. Discussion started: 19 March 2024

References

ACS2021: Remote Pilot – Small Unmanned Aircraft Systems: Airman Certification Standards, Federal Aviation Administration, Flight Standards Service Washington, DC 20591, fAA-S-ACS-10B, 2021.

Alexe, M., Bergamaschi, P., Segers, A., Detmers, R., Butz, A., Hasekamp, O., Guerlet, S., Parker, R., Boesch, H., Frankenberg, C., Scheepmaker, R. A., Dlugokencky, E., Sweeney, C., Wofsy, S. C., and Kort, E. A.: Inverse modelling of CH4 emissions for 2010-2011 using different satellite retrieval products from GOSAT and SCIAMACHY, Atmospheric Chemistry and Physics, 15, 113–133, https://doi.org/https://doi.org/10.5194/acp-15-113-2015, 2015.

Bhattacharya, R.: Atmospheric Dispersion, Atomic Energy Regulatory Board, https://ansn.iaea.org/Common/Topics/OpenTopic.aspx?ID=13012, 2013.

Bogner, J. and Matthews, E.: Global methane emissions from landfills: New methodology and annual estimates 1980-1996, Global Biogeochemical Cycles, 17, https://doi.org/https://doi.org/10.1029/2002GB001913, 2003.

Cheewaphongphan, P., Chatani, S., and Saigusa, N.: Exploring Gaps between Bottom-Up and Top-Down Emission Estimates Based on Uncertainties in Multiple Emission Inventories: A Case Study on CH4 Emissions in China, Sustainability, 11, https://doi.org/https://doi.org/10.3390/su11072054, 2019.

Chen, J., Viatte, C., Hedelius, J. K., Jones, T., Franklin, J. E., Parker, H. A., Gottlieb, E. W., Wennberg, P. O., Dubey, M. K., and Wofsy, S. C.: Differential column measurements using compact solar-tracking spectrometers, Atmospheric Chemistry and Physics, 16, 8479–8498, https://doi.org/https://doi.org/10.5194/acp-16-8479-2016, 2016.

DJIM600P2018: Matrice 600 Pro User Manual, Dà Jiāng Innovations, v1.0 edn., https://www.dji.com/matrice600-pro/info#downloads, 2018.

Duren, R. M., Thorpe, A. K., Foster, K. T., Rafiq, T., Hopkins, F. M., Yadav, V., Bue, B. D., Thompson, D. R., Conley, S. A., Colombi, N. K., Frankenberg, C., McCubbin, I. B., Eastwood, M. L., Falk, M., Herner, J. D., Croes, B. E., Green, R. O., and Miller, C. E.: California's methane super-emitters, Nature, 575, 180–184, https://doi.org/https://doi.org/10.1038/s41586-019-1720-3, 2019.

El Abbadi, S. H., Chen, Z., Burdeau, P. M., Rutherford, J. S., Chen, Y., Zhang, Z., Sherwin, E. D., and Brandt, A. R.: Comprehensive evaluation of aircraft-based methane sensing for greenhouse gas mitigation, https://doi.org/https://doi.org/10.31223/X51D4C, this is a Preprint and has not been peer reviewed. This is version 3 of this Preprint, 2023.

Etiope, G. and Lollar, B.: Abiotic methane on Earth, Reviews of Geophysics, 51, https://doi.org/https://doi.org/10.1002/rog.20011, 2013.

Follansbee, E., Dubey, M. L., Dooley, J. F., Schuck, C., Minschwaner, K., Biraud, S. C., Lee, J. E., and Dubey, M. K.: Gaussian Plume Inversions of Methane Emissions from an Orphan Well using Ambient Observations: Are They Good Enough?, preprint, 2024.

Forster, P., Ramaswamy, V., Artaxo, P., Berntsen, T., Betts, R., Fahey, D. W., Haywood, J., Lean, J., Lowe, D. C., Myhre, G., Nganga, J., Prinn, R., Raga, G., Schulz, M., and Van Dorland, R.: Changes in Atmospheric Constituents and in Radiative Forcing, chap. 2, pp. 130–234, Geneva: Intergovernmental Panel on Climate Change, http://www.ipcc.ch/ipccreports/ar4-wg1.htm, 2007.

Frankenberg, C., Meirink, J. F., van Weele, M., Platt, U., and Wagner, T.: Assessing Methane Emissions from Global Space-Borne Observations, Science, 308, 1010–1014, https://doi.org/https://doi.org/10.1126/science.1106644, 2005.

Frankenberg, C., Thorpe, A. K., Thompson, D. R., Hulley, G., Kort, E. A., Vance, N., Jakob, B., Krings, T., Gerilowski, K., Sweeney, C., Conley, S. A., Bue, B. D., Aubrey, A. D., Hook, S., and Green, R. O.: Airborne methane remote measurements reveal heavy-tail flux distribution in Four Corners region, Proceedings of the National Academy of Sciences, 113, 9734–9739, https://doi.org/https://doi.org/10.1073/pnas.1605617113, 2016.

https://doi.org/10.5194/egusphere-2024-760
Preprint. Discussion started: 19 March 2024

Gisi, M., Hase, F., Dohe, S., Blumenstock, T., Simon, A., and Keens, A.: XCO_2-measurements with a tabletop FTS using solar absorption spectroscopy, Atmospheric Measurement Techniques, 5, 2969–2980, https://doi.org/https://doi.org/10.5194/amt-5-2969-2012, 2012.

Glasby, G. P.: Abiogenic Origin of Hydrocarbons: An Historical Overview, Resource Geology, 56, 83–96, https://doi.org/https://doi.org/10.1111/j.1751-3928.2006.tb00271.x, 2006.

Hansen, J., Sato, M., Ruedy, R., Lacis, A., and Oinas, V.: Global warming in the twenty-first century: An alternative scenario, Proceedings of the National Academy of Sciences, 97, 9875–9880, https://doi.org/https://doi.org/10.1073/pnas.170278997, 2000.

Heath, G. A., Warner, E., Steinberg, D., and Brandt, A. R.: Estimating U.S. Methane Emissions from the Natural Gas Supply Chain: Approaches, Uncertainties, Current Estimates, and Future Studies, Tech. rep., Joint Institute for Strategic Energy Analysis, https://doi.org/https://doi.org/10.2172/1226158, 2015.

Heerah, S., Frausto-Vicencio, I., Jeong, S., Marklein, A. R., Ding, Y., Meyer, A. G., Parker, H. A., Fischer, M. L., Franklin, J. E., Hopkins, F. M., and Dubey, M. K.: Dairy Methane Emissions in California's San Joaquin Valley Inferred With Ground-Based Remote Sensing Observations in the Summer and Winter, Journal of Geophysical Research: Atmospheres, 126, e2021JD034 785, https://doi.org/https://doi.org/10.1029/2021JD034785, e2021JD034785 2021JD034785, 2021.

Hiller, R. V., Neininger, B., Brunner, D., Gerbig, C., Bretscher, D., Künzle, T., Buchmann, N., and Eugster, W.: Aircraft-Based CH4 flux estimates for validation of emissions from an agriculturally dominated area in Switzerland, Journal of Geophysical Research: Atmospheres, 119, 4874–4887, https://doi.org/https://doi.org/10.1002/2013JD020918, 2014.

Hodnebrog, Ø., Dalsøren, S. B., and Myhre, G.: Lifetimes, direct and indirect radiative forcing, and global warming potentials of ethane (C2H6), propane (C3H8), and butane (C4H10), Atmospheric Science Letters, 19, e804, https://doi.org/https://doi.org/10.1002/asl.804, 2018.

Hollenbeck, D., Nunez, G., Christensen, L. E., and Chen, Y.: Wind Measurement and Estimation with Small Unmanned Aerial Systems (sUAS) Using On-Board Mini Ultrasonic Anemometers, in: 2018 International Conference on Unmanned Aircraft Systems (ICUAS), pp. 285–292, https://doi.org/https://doi.org/10.1109/ICUAS.2018.8453418, 2018.

Holmes, C. D., Prather, M. J., Søvde, O. A., and Myhre, G.: Future methane, hydroxyl, and their uncertainties: key climate and emission parameters for future predictions, Atmospheric Chemistry and Physics, 13, 285–302, https://doi.org/https://doi.org/10.5194/acp-13-285-2013, 2013.

Jacob, D. J., Varon, D. J., Cusworth, D. H., Dennison, P. E., Frankenberg, C., Gautam, R., Guanter, L., Kelley, J., McKeever, J., Ott, L. E., Poulter, B., Qu, Z., Thorpe, A. K., Worden, J. R., and Duren, R. M.: Quantifying methane emissions from the global scale down to point sources using satellite observations of atmospheric methane, Atmospheric Chemistry and Physics, 22, 9617–9646, https://doi.org/https://doi.org/10.5194/acp-22-9617-2022, 2022.

Johnson, D., Heltzel, R., and Oliver, D.: Temporal Variations in Methane Emissions from an Unconventional Well Site, ACS Omega, 4, 3708–3715, https://doi.org/https://doi.org/10.1021/acsomega.8b03246, pMID: 31459583, 2019.

Karion, A., Sweeney, C., Pétron, G., Frost, G., Hardesty, R. M., Kofler, J., Miller, B. R., Newberger, T., Wolter, S., Banta, R., Brewer, A., Dlugokencky, E., Lang, P., Montzka, S. A., Schnell, R., Tans, P., Trainer, M., Zamora, R., and Conley, S. A.: Methane emissions estimate from airborne measurements over a western United States natural gas field, Geophysical Research Letters, 40, 4393–4397, https://doi.org/https://doi.org/10.1002/grl.50811, 2013.

Karion, A., Sweeney, C., Kort, E. A., Shepson, P. B., Brewer, A., Cambaliza, M., Conley, S. A., Davis, K., Deng, A., Hardesty, M., Herndon, S. C., Lauvaux, T., Lavoie, T. N., Lyon, D. R., Newberger, T., Pétron, G., Rella, C., Smith, M., Wolter, S., Yacovitch, T. I., and Tans, P.:

https://doi.org/10.5194/egusphere-2024-760
Preprint. Discussion started: 19 March 2024

Aircraft-Based Estimate of Total Methane Emissions from the Barnett Shale Region, Environmental Science & Technology, 49, 8124–8131, https://doi.org/https://doi.org/10.1021/acs.est.5b00217, pMID: 26148550, 2015.

Kort, E. A., Frankenberg, C., Costigan, K. R., Lindenmaier, R., Dubey, M. K., and Wunch, D.: Four corners: The largest US methane anomaly viewed from space, Geophysical Research Letters, 41, 6898–6903, https://doi.org/https://doi.org/10.1002/2014GL061503, 2014.

Kutcherov, V. G. and Krayushkin, V. A.: Deep-seated abiogenic origin of petroleum: From geological assessment to physical theory, Reviews of Geophysics, 48, https://doi.org/https://doi.org/10.1029/2008RG000270, 2010.

Lan, X., Talbot, R., Laine, P., and Torres, A.: Characterizing Fugitive Methane Emissions in the Barnett Shale Area Using a Mobile Laboratory, Environmental Science & Technology, 49, 8139–8146, https://doi.org/10.1021/es5063055, pMID: 26148552, 2015.

Lavoie, T. N., Shepson, P. B., Cambaliza, M. O. L., Stirm, B. H., Karion, A., Sweeney, C., Yacovitch, T. I., Herndon, S. C., Lan, X., and Lyon, D. R.: Aircraft-Based Measurements of Point Source Methane Emissions in the Barnett Shale Basin, Environmental Science & Technology, 49, 7904–7913, https://doi.org/https://doi.org/10.1021/acs.est.5b00410, pMID: 26148549, 2015.

Lavoie, T. N., Shepson, P. B., Cambaliza, M. O. L., Stirm, B. H., Conley, S. A., Mehrotra, S., Faloona, I. C., and Lyon, D. R.: Spatio-temporal Variability of Methane Emissions at Oil and Natural Gas Operations in the Eagle Ford Basin, Environmental Science & Technology, 51, 8001–8009, https://doi.org/https://doi.org/10.1021/acs.est.7b00814, pMID: 28678487, 2017.

McKinney, K. A., Wang, D., Ye, J., Fouchier, J.-B., Guimar
textasciitilde aes, P. C., Batista, C. E., Souza, R. A. F., Alves, E. G., Gu, D., Guenther, A. B., and Martin, S. T.: A sampler for atmospheric volatile organic compounds by copter unmanned aerial vehicles, Atmospheric Measurement Techniques, 12, 3123–3135, https://doi.org/https://doi.org/10.5194/amt-12-3123-2019, 2019.

Meyer, A. G., Lindenmaier, R., Heerah, S., Benedict, K. B., Kort, E. A., Peischl, J., and Dubey, M. K.: Using Multiscale Ethane/Methane Observations to Attribute Coal Mine Vent Emissions in the San Juan Basin From 2013 to 2021, Journal of Geophysical Research: Atmospheres, 127, e2022JD037 092, https://doi.org/https://doi.org/10.1029/2022JD037092, e2022JD037092 2022JD037092, 2022.

MIRAManual2019: MIRA Pico Mobile LDS: Natural Gas Leak Detection System w/GPS, Aeris Technologies, Inc, https://0f0d05.a2cdn1.secureserver.net/wp-content/uploads/2019/12/MIRA-PicoMobile-LDS_191208_FINAL_quartz.pdf, www.aerissensors.com, 2019.

NAS2018: Thriving on Our Changing Planet: A Decadal Strategy for Earth Observation from Space, The National Academies Press, ISBN 9780309467575, https://doi.org/https://doi.org/10.17226/24938, 2018.

Olaguer, E. P., Jeltema, S., Gauthier, T., Jermalowicz, D., Ostaszewski, A., Batterman, S., Xia, T., Raneses, J., Kovalchick, M., Miller, S., Acevedo, J., Lamb, J., Benya, J., Wendling, A., and Zhu, J.: Landfill Emissions of Methane Inferred from Unmanned Aerial Vehicle and Mobile Ground Measurements, Atmosphere, 13, https://doi.org/https://doi.org/10.3390/atmos13060983, 2022.

Parker, R., Boesch, H., Cogan, A., Fraser, A., Feng, L., Palmer, P. I., Messerschmidt, J., Deutscher, N., Griffith, D. W. T., Notholt, J., Wennberg, P. O., and Wunch, D.: Methane observations from the Greenhouse Gases Observing SATellite: Comparison to ground-based TCCON data and model calculations, Geophysical Research Letters, 38, https://doi.org/https://doi.org/10.1029/2011GL047871, 2011.

Peischl, J., Eilerman, S. J., Neuman, J. A., Aikin, K. C., Gouw, J., Gilman, J. B., Herndon, S. C., Nadkarni, R., Trainer, M., Warneke, C., and Ryerson, T. B.: Quantifying Methane and Ethane Emissions to the Atmosphere From Central and Western U.S. Oil and Natural Gas Production Regions, Journal of Geophysical Research: Atmospheres, 123, 7725–7740, https://doi.org/https://doi.org/10.1029/2018JD028622, 2018.

Scherer, J. J.: Next-Generation Laser-Based Natural Gas Leak Detection, https://www.epa.gov/sites/default/files/2017-11/documents/16.scherer.aeris_2017aiw.pdf, ePA STAR Webinar, 2017.

https://doi.org/10.5194/egusphere-2024-760
Preprint. Discussion started: 19 March 2024

Schneising, O., Buchwitz, M., Reuter, M., Vanselow, S., Bovensmann, H., and Burrows, J. P.: Remote sensing of methane leakage from natural gas and petroleum systems revisited, Atmospheric Chemistry and Physics, 20, 9169–9182, https://doi.org/https://doi.org/10.5194/acp-20-9169-2020, 2020.

Schwietzke, S., Pétron, G., Conley, S. A., Pickering, C., Mielke-Maday, I., Dlugokencky, E. J., Tans, P. P., Vaughn, T., Bell, C., Zimmerle, D., Wolter, S., King, C. W., White, A. B., Coleman, T., Bianco, L., and Schnell, R. C.: Improved Mechanistic Understanding of Natural Gas Methane Emissions from Spatially Resolved Aircraft Measurements, Environmental Science & Technology, 51, 7286–7294, https://doi.org/https://doi.org/10.1021/acs.est.7b01810, pMID: 28548824, 2017.

Seinfeld, J. and Pandis, S.: Atmospheric Diffusion, chap. 18, pp. 828–899, A Wiley-Interscience publication, Wiley, ISBN 9780471720171, https://books.google.co.uk/books?id=tZEpAQAAMAAJ, 2006.

Shah, A., Allen, G., Pitt, J. R., Ricketts, H., Williams, P. I., Helmore, J., Finlayson, A., Robinson, R., Kabbabe, K., Hollingsworth, P., Rees-White, T. C., Beaven, R., Scheutz, C., and Bourn, M.: A Near-Field Gaussian Plume Inversion Flux Quantification Method, Applied to Unmanned Aerial Vehicle Sampling, Atmosphere, 10, https://doi.org/https://doi.org/10.3390/atmos10070396, 2019.

Sherwin, E. D., El Abbadi, S. H., Burdeau, P. M., Zhang, Z., Chen, Z., Rutherford, J. S., Chen, Y., and Brandt, A. R.: Single-blind test of nine methane-sensing satellite systems from three continents, https://doi.org/https://doi.org/10.31223/X56089, this is a Preprint and has not been peer reviewed. This is version 1 of this Preprint., 2023.

Simpson, I. J., Andersen, M. P. S., Meinardi, S., Bruhwiler, L., Blake, N. J., Helmig, D., Rowland, F. S., and Blake, D. R.: Long-term decline of global atmospheric ethane concentrations and implications for methane, Nature, 488, 490–494, https://doi.org/https://doi.org/10.1038/nature11342, 2012.

Song, C., Zhu, J.-J., Willis, J. L., Moore, D. P., Zondlo, M. A., and Ren, Z. J.: Methane Emissions from Municipal Wastewater Collection and Treatment Systems, Environmental Science & Technology, 57, 2248–2261, https://doi.org/10.1021/acs.est.2c04388, pMID: 36735881, 2023.

Stockie, J. M.: The Mathematics of Atmospheric Dispersion Modeling, SIAM Review, 53, 349–372, https://doi.org/https://doi.org/10.1137/10080991X, 2011.

Stolper, D. A., Lawson, M., Formolo, M. J., Davis, C. L., Douglas, P. M. J., and Eiler, J. M.: The utility of methane clumped isotopes to constrain the origins of methane in natural gas accumulations, Geological Society, London, Special Publications, 468, 23–52, https://doi.org/https://doi.org/10.1144/SP468.3, 2018.

Travis, B., Dubey, M., and Sauer, J.: Neural networks to locate and quantify fugitive natural gas leaks for a MIR detection system, Atmospheric Environment: X, 8, 100 092, https://doi.org/https://doi.org/10.1016/j.aeaoa.2020.100092, 2020.

TWSDatasheet2022: World's Smallest & Lightest 3D Ultrasonic Anemometer, Anemoment, LLC, https://anemoment.com/resources/#downloads, 2022.

TWSManual2018: Trisonica Mini User Manual, Anemoment, LLC, https://anemoment.com/resources/#downloads, 2018.

Vaughn, T. L., Bell, C. S., Pickering, C. K., Schwietzke, S., Heath, G. A., Pétron, G., Zimmerle, D. J., Schnell, R. C., and Nummedal, D.: Temporal variability largely explains top-down/bottom-up difference in methane emission estimates from a natural gas production region, Proceedings of the National Academy of Sciences, 115, 11 712–11 717, https://doi.org/https://doi.org/10.1073/pnas.1805687115, 2018.

Viatte, C., Lauvaux, T., Hedelius, J. K., Parker, H. A., Chen, J., Jones, T., Franklin, J. E., Deng, A. J., Gaudet, B., Verhulst, K., Duren, R., Wunch, D., Roehl, C., Dubey, M. K., Wofsy, S. C., and Wennberg, P. O.: Methane emissions from dairies in the Los Angeles Basin, Atmospheric Chemistry and Physics, 17, 7509–7528, https://doi.org/https://doi.org/10.5194/acp-17-7509-2017, 2017.

https://doi.org/10.5194/egusphere-2024-760
Preprint. Discussion started: 19 March 2024

Villa, T. F., Gonzalez, F., Miljievic, B., Ristovski, Z. D., and Morawska, L.: An Overview of Small Unmanned Aerial Vehicles for Air Quality Measurements: Present Applications and Future Prospectives, Sensors, 16, https://doi.org/https://doi.org/10.3390/s16071072, 2016.

Woodward, J.: Estimating the Flammable Mass of a Vapor Cloud, A CCPS Concept Book, Wiley, ISBN 9780470935354, https://books.google.co.uk/books?id=31DexdyRIKAC, 2010.